INTERFACE

royalsocietypublishing.org/journal/rsif

Research

Cite this article: McCormack CP, Yan AWC, Brown JC, Sukhova K, Peacock TP, Barclay WS, Dorigatti I. 2023 Modelling the viral dynamics of the SARS-CoV-2 Delta and Omicron variants in different cell types. *J. R. Soc. Interface* **20**: 20230187.
https://doi.org/10.1098/rsif.2023.0187

Received: 30 March 2023
Accepted: 18 July 2023

Subject Category:
Life Sciences–Mathematics interface

Subject Areas:
biomathematics, computational biology

Keywords:
SARS-CoV-2, viral dynamics, viral kinetics model, Omicron, Delta

Authors for correspondence:
Clare P. McCormack
e-mail: c.mccormack14@imperial.ac.uk
Ada W. C. Yan
e-mail: a.yan@imperial.ac.uk

†These authors contributed equally to this study.

Electronic supplementary material is available online at https://doi.org/10.6084/m9.figshare.c.6753889.

THE ROYAL SOCIETY PUBLISHING

Modelling the viral dynamics of the SARS-CoV-2 Delta and Omicron variants in different cell types

Clare P. McCormack[1,†], Ada W. C. Yan[2,†], Jonathan C. Brown[2], Ksenia Sukhova[2], Thomas P. Peacock[2], Wendy S. Barclay[2] and Ilaria Dorigatti[1]

[1]MRC Centre for Global Infectious Disease Analysis, School of Public Health, and [2]Department of Infectious Disease, Imperial College London, London, UK

CPM, 0000-0003-1371-8401; AWCY, 0000-0001-7456-339X; JCB, 0000-0001-6849-3962; KS, 0000-0003-3678-5631; TPP, 0000-0001-7077-2928; WSB, 0000-0002-3948-0895

We use viral kinetic models fitted to viral load data from *in vitro* studies to explain why the SARS-CoV-2 Omicron variant replicates faster than the Delta variant in nasal cells, but slower than Delta in lung cells, which could explain Omicron's higher transmission potential and lower severity. We find that in both nasal and lung cells, viral infectivity is higher for Omicron but the virus production rate is higher for Delta, with an estimated approximately 200-fold increase in infectivity and 100-fold decrease in virus production when comparing Omicron with Delta in nasal cells. However, the differences are unequal between cell types, and ultimately lead to the basic reproduction number and growth rate being higher for Omicron in nasal cells, and higher for Delta in lung cells. In nasal cells, Omicron alone can enter via a TMPRSS2-independent pathway, but it is primarily increased efficiency of TMPRSS2-dependent entry which accounts for Omicron's increased activity. This work paves the way for using within-host mathematical models to understand the transmission potential and severity of future variants.

1. Introduction

Since its designation as a variant of concern (VOC) by the World Health Organization on 26 November 2021 [1], the Omicron (B.1.1.529\BA.1) variant of severe acute respiratory coronavirus 2 (SARS-CoV-2) has rapidly displaced the Delta (B.1.617.2) variant to become the dominant SARS-CoV-2 variant globally [2–4]. Analyses have demonstrated that Omicron can partially evade the immunity generated through previous infection and vaccination [5–8], thereby leading to reduced vaccine effectiveness against symptomatic disease [9].

Despite this reduction in vaccine effectiveness against symptomatic disease, the risk of severe outcomes (including hospital admission and death) following infection with Omicron is substantially lower than following infection with Delta, for both vaccinated and unvaccinated individuals [10,11] (although one study reported similar case fatality ratios between the two variants in unvaccinated individuals without previous infection [12]). While much remains to be understood about the mechanisms underpinning this observation, a reduction in the capacity of Omicron relative to Delta to replicate in lung cells has been suggested as a possible explanation [13]. On the other hand, Omicron's increased ability to replicate in nasal cells has been suggested as an explanation for Omicron's transmission advantage over Delta observed from epidemiological data [14–16].

It has been hypothesized that these differences in viral replication capacity in different cells can be attributed to how Omicron and Delta use different pathways to enter host cells [13,14,17,18]. All SARS-CoV-2 viruses can enter cells which

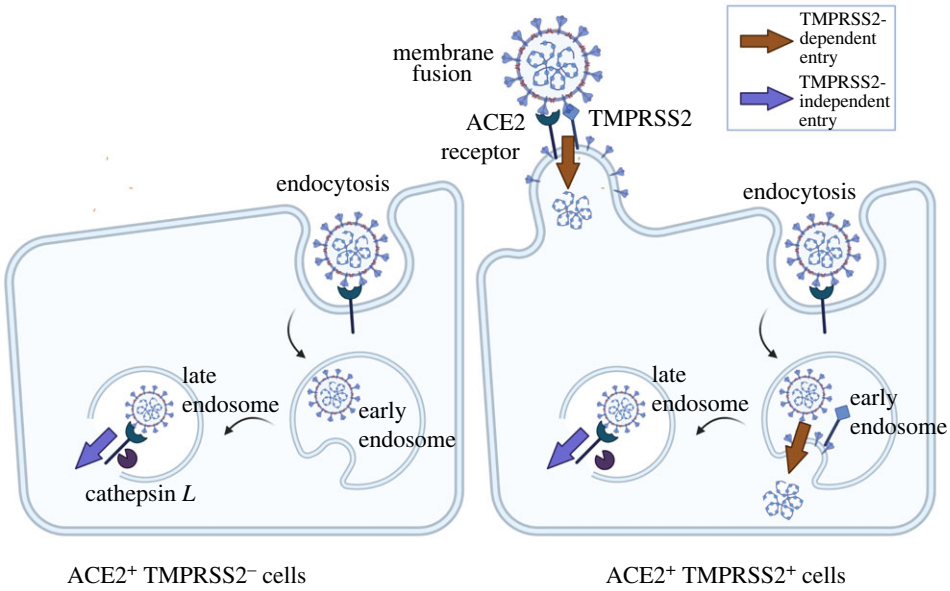

Figure 1. Illustration of TMPRSS2-dependent and TMPRSS2-independent entry pathways and their inhibition by endosomal restriction factors. In ACE2+ TMPRSS2+ cells (right), virus can enter in a TMPRSS2-dependent way via membrane fusion either at the cell surface or the early endosome; alternatively, virus can enter in a TMPRSS2-independent way through the late endosome. In ACE2+ TMPRSS2− cells (left), only the TMPRSS2-independent pathway is available. Both pathways can be inhibited by endosomal restriction factors. Created with BioRender.com.

express both ACE2 and TMPRSS2 proteins, via fusion of the viral and cell membranes or via early endosomes [19]. However, Omicron is also able to efficiently enter ACE2+ cells via fusion from the endosome after endocytosis, without the involvement of TMPRSS2 [14,20]. This could expand the range of cells that Omicron can infect. A complication is, by entering cells via the endosome, SARS-CoV-2 may be inhibited by endosomal restriction factors such as interferon-induced transmembrane (IFITM) proteins [21,22] or NCOA7 [23]. Understanding how these virological properties shape the viral dynamics of SARS-CoV-2 in different cell types can enhance our understanding of the mechanisms underlying the observed differences in transmissibility between the Omicron and Delta variants. The different entry pathways and their inhibition by endosomal restriction factors are shown in figure 1.

Mechanistic mathematical models, calibrated against virological data, are a powerful tool for exploring viral dynamics as they provide a framework to quantify key characteristics of different variants and build an understanding of the drivers of inter-individual variation in response to infection. Previous within-host modelling studies of SARS-CoV-2 have enabled an understanding of the effect of covariates such as age, sex and disease severity on viral load [24], the degree of heterogeneity between individuals [25], the association between viral dynamics and mortality in hospitalized patients [26], the pathogenesis of infection [27], and the potential effect of antivirals and masking on viral load [28–36]. Models fitted to data from vaccine trials have suggested correlates of protection [37], while more theoretical immunological models have also been developed with the ultimate aim of understanding the interplay between the immune response and disease severity [38–40]. Studies linking the within- and between-host scales have improved the understanding of the relationship between cycle threshold (Ct) values and infectiousness [25,41], the role of super-spreader events [42], suggested characteristics of optimal testing regimes [43], and provided explanations for population-level epidemiological observations, e.g. the apparent reduction in viral load observed during the declining phase of an epidemic [44].

The studies mentioned above have all fitted their models to data from *in vivo* studies. While dynamics in humans are of ultimate interest, modelling viral kinetics and the immune response *in vivo* is extremely complex. Moreover, studies in humans are often limited, with little or no information on the timing and amount of the viral inoculum, sparse longitudinal observations and often no available measurements before the start of symptom onset [25,41]. *In vitro* studies offer a simplification of *in vivo* dynamics, where both the inoculum and method of inoculation is controlled, and where some components of the immune response—such as the adaptive immune response—are eliminated. Viral load can be measured from the start of infection, which is important for estimating the growth rate and basic reproduction number of the virus, which in turn can be used to assess the potential for new variants to outcompete existing variants.

Here, using viral kinetics models calibrated against viral replication data generated through experimental infection studies in primary human nasal epithelial cells (hNECs) and immortalized Calu-3 lung cells, we characterize and compare the dynamics of Omicron and Delta viruses in each cell type by quantifying key properties such as the basic reproduction number and growth rate, and by exploring how these properties vary for different entry pathways, in the presence and absence of functional endosomal restriction factors.

2. Material and methods

2.1. Experimental design/data

Full details of the viral kinetics experiments conducted are provided in Peacock *et al.* [20]. In brief, Calu-3 and primary human nasal epithelial cells (hNECs) were inoculated with Omicron BA.1 and Delta/B.1.617.2 isolates at a multiplicity of infection (MOI) of 0.001 (Calu-3) or 0.05 (hNECs), and incubated for 1 h at 37°C. The inoculum was then removed and, in the case

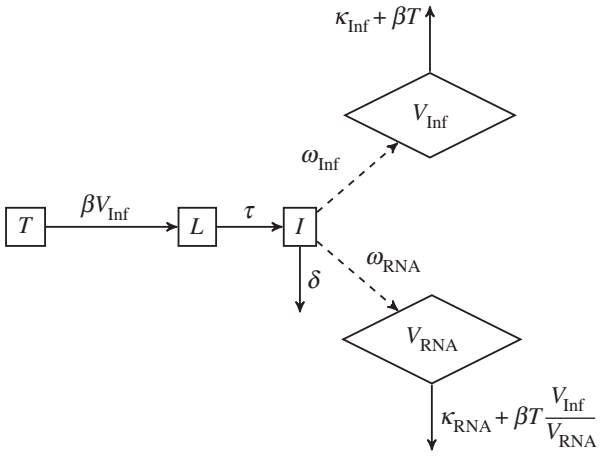

Figure 2. Compartmental diagram of Model 1. Target cells T become infected at a rate β per infectious virion (V_{Inf}). Following an eclipse phase of mean duration of $1/\tau$ days, infectious cells (I) produce infectious virus as measured by plaque-assay (V_{Inf}) and total virus as measured by qPCR (V_{RNA}) at rates ω_{Inf} and ω_{RNA}, respectively. Infected cells have a mean lifespan of $1/\delta$ days, and infectious and total virus are assumed to decay at rates κ_{Inf} and κ_{RNA}, respectively.

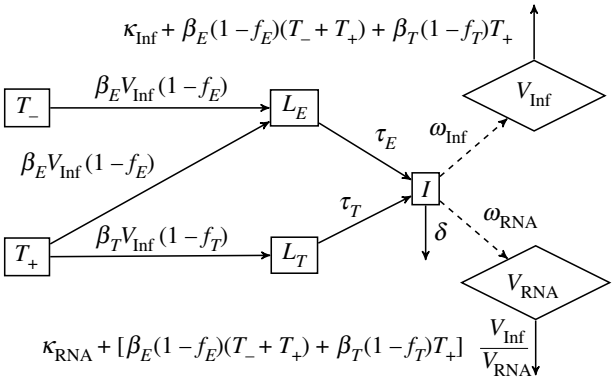

Figure 3. Compartmental diagram for Model 2. ACE2$^+$ TMPRSS2$^-$ target cells (T_) become infected through TMPRSS2-independent pathways at a rate β_E per infectious virion (V_{Inf}). ACE2$^+$ TMPRSS2$^+$ target cells (T_+) become infected through TMPRSS2-independent pathways at a rate β_E per infectious virion, and through TMPRSS2-dependent pathways at a rate β_T per infectious virion. Endosomal restriction factors decrease the infectivity through TMPRSS2-independent pathways by a factor f_E, and through TMPRSS2-dependent pathways by a factor f_T. Cells infected through TMPRSS2-independent and TMPRSS2-dependent pathways (L_E and L_T respectively) undergo eclipse phases of mean duration $1/\tau_E$ and $1/\tau_T$ days, respectively. Following the eclipse phase, infectious cells (I) behave as per Model 1.

of Calu-3 cells, replaced with 1 ml serum-free Dulbecco's modified eagle medium (DMEM). For Calu-3 cells, 100 µl of supernatant was collected for titration at 18, 24, 48 and 72 h post-infection. For hNECs, at the same time points post-infection, the supernatant was collected by adding 200 µl of serum-free DMEM to the apical surface, incubating for 10 min and removing for collection.

Additional experiments were performed to investigate the effect of Camostat mesylate (henceforth referred to as Camostat) and Amphotericin B on viral kinetics. Camostat is a serine protease inhibitor and thus inhibits TMPRSS2, while Amphotericin B inhibits the restriction of viral endosomal entry by endosomal restriction factors such as IFITM proteins [45–47]. Cells were pretreated both basolaterally and apically with either 50 µM of Camostat, 1 µM of Amphotericin B, or no drug for 2 h prior to infection, and this concentration of drug was maintained in the basolateral media throughout the experiment. Infections and collection of time points were performed as above.

All experiments were performed in triplicate. Infectious viral titres were quantified by plaque assay and viral genome numbers were quantified by E gene reverse transcription quantitative polymerase chain reaction (RT-qPCR).

2.2. Mathematical models

2.2.1. Model 1

To gain an initial understanding of the differences between the observed infection dynamics of the Omicron and Delta variants in each cell type (in the absence of drugs modulating cell entry pathways), we first developed a simple model of the viral dynamics which assumed a single virus entry pathway for both variants. A simple schematic of the model is provided in figure 2. Model equations are in the electronic supplementary material.

Target cells T become infected at a rate β (target cell infection rate) per infectious virion (V_{Inf}). The target cell infection rate is defined as the proportion of cells infected per day, per unit inoculum of 1 plaque forming unit (pfu) ml^{-1}. Following an eclipse phase of mean duration of $1/\tau$ days, infectious cells (I) produce infectious and non-infectious virus. Infectious virus (V_{Inf}), as measured by plaque-assay, and total (infectious and non-infectious) virus (V_{RNA}), as measured by RT-qPCR, are produced at rates ω_{Inf} and ω_{RNA} respectively. (While the RT-qPCR assay could detect viral RNA released from lysed cells as well as from extracellular viral particles, the model assumes that all detected viral RNA originates from viral particles.) The duration of the eclipse phase $1/\tau$ reflects the speed of a single viral replication cycle, whereas the rate of viral production ω_{Inf} also reflects replication capacity. Infectious cells have a mean lifespan of $1/\delta$ days, and infectious and non-infectious virus is assumed to decay at rates κ_{Inf} and κ_{RNA}, respectively, with additional loss due to entry into cells. Cells which express the ACE2 receptor, which is required for SARS-CoV-2 virus entry, are considered target cells.

The basic reproduction number (R_0) for Model 1 is defined as the mean number of infected cells produced by each infected cell over its lifespan at disease-free conditions (at the start of infection, time t^*) and is given by

$$R_0 = \frac{\beta T^* \omega_{Inf}}{\delta(\kappa_{Inf} + \beta T^*)},$$

where T^* is the initial number of target cells. The initial growth rate (r) is obtained by calculating the largest eigenvalue of the Jacobian matrix obtained when linearizing the model equations around the disease-free equilibrium. Further details are provided in the electronic supplementary material.

2.2.2. Model 2

The experimental data showed that while Delta can only enter ACE2$^+$ cells by using the TMPRSS2 protein, Omicron can enter these cells through both TMPRSS2-dependent and TMPRSS2-independent pathways. Thus, in Model 2, we modify Model 1 to account for the two possible cell entry pathways, where TMPRSS2-independent pathways can be used to infect all ACE2$^+$ cells, and TMPRSS2-dependent pathways can only infect ACE2$^+$ TMPRSS2$^+$ cells. We assume that all ACE2$^+$ cells become infected through TMPRSS2-independent pathways at a rate β_E per infectious virion (V_{Inf}) and that ACE2$^+$ TMPRSS2$^+$ target cells (T_+) also become infected through TMPRSS2-dependent pathways at a rate β_T per infectious virion. We assume that endosomal restriction factors decrease the infectivity through the TMPRSS2-independent pathways by a factor f_E, and through TMPRSS2-dependent pathways by a factor f_T. Cells infected through TMPRSS2-independent and TMPRSS2-dependent pathways

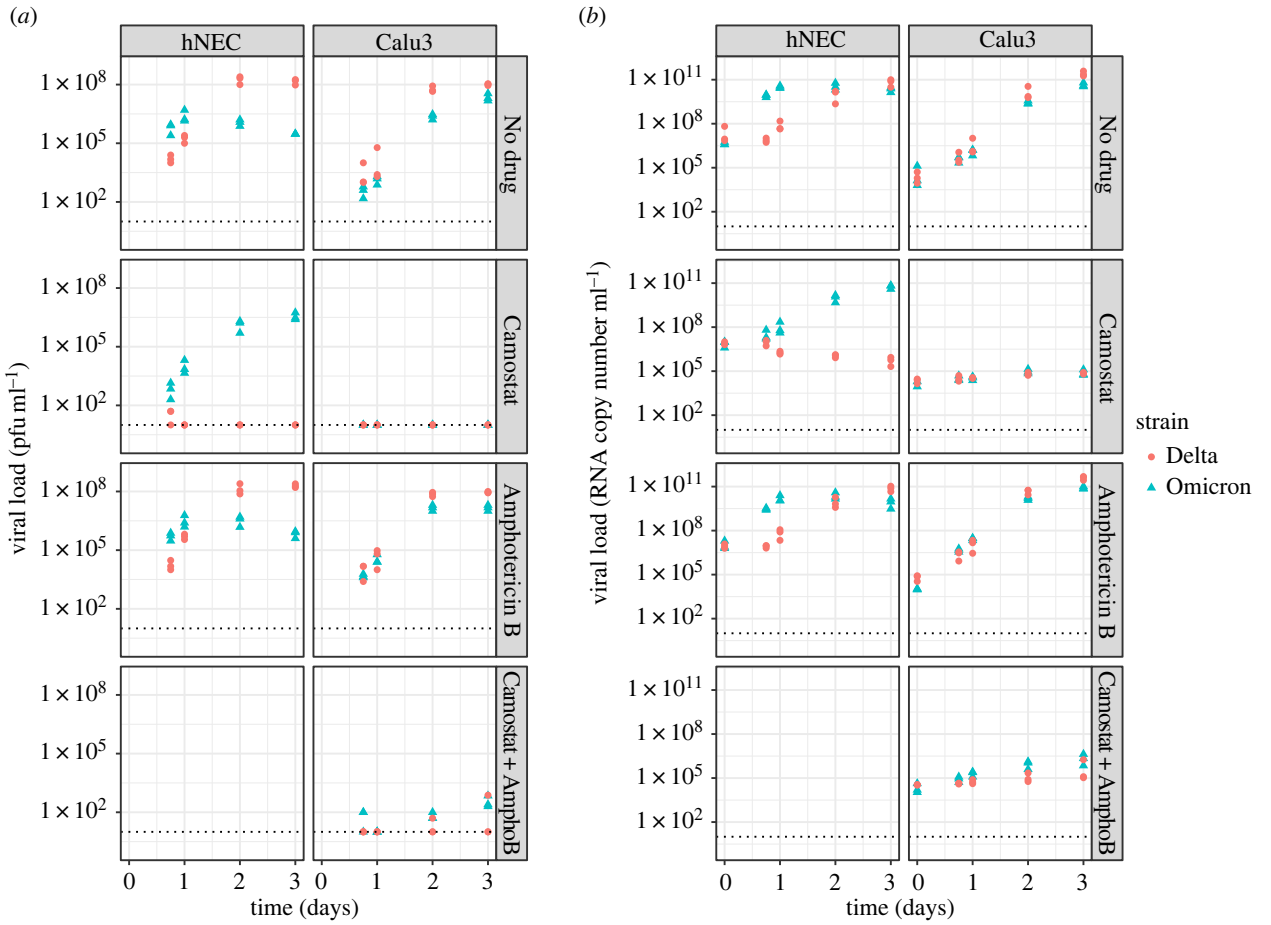

Figure 4. Summary of data. (*a*) Infectious viral load (pfu ml^{-1}) quantified by plaque assay and (*b*) RNA copy number ml^{-1} quantified by RT-qPCR for Omicron (blue triangles) and Delta (red dots) for different cell types (columns) and drug treatments (rows). The dotted line shows the limit of detection; markers on the lines represent measurements below the limit of detection. Cells were infected on day 0.

(L_E and L_T, respectively) undergo eclipse phases of mean duration $1/\tau_E$ and $1/\tau_T$ days, respectively. Following the eclipse phase, infectious cells (I) behave as per Model 1. The flow diagram of Model 2 is described in figure 3.

The basic reproduction number for Model 2 is given by

$$R_0 = \frac{[\beta_E(1-f_E)T_-^* + \beta_E(1-f_E)T_+^* + \beta_T(1-f_T)T_+^*]\omega_{\text{Inf}}}{\delta[\kappa_{\text{Inf}} + \beta_E(1-f_E)T_-^* + \beta_E(1-f_E)T_+^* + \beta_T(1-f_T)T_+^*]}.$$

We also define pathway-specific R_0s. R_{0E} is the number of infectious virions produced by one infectious virus, if only the TMPRSS2-independent pathway were active; it is computed by setting $\beta_T = 0$ in the above definition of R_0. Similarly, R_{0T} is the number of infectious virions produced by one infectious virus, if only the TMPRSS2-dependent pathway were active; it is computed by setting $\beta_E = 0$ in the above definition of R_0. Pathway-specific growth rates are determined similarly.

In addition, we can define both pathway-specific and overall R_0 in the absence of IFITM, denoted R_{0EX}, R_{0TX} and R_{0X} by setting $f_E = f_T = 0$. For example,

$$R_{0EX} = \frac{[\beta_E T_-^* + \beta_E T_+^*]\omega_{\text{Inf}}}{\delta[\kappa_{\text{Inf}} + \beta_E T_-^* + \beta_E T_+^*]}.$$

Model 2 is fitted to hNEC and Calu-3 data without drug, in the presence of Camostat, in the presence of Amphotericin B and in the presence of both drugs. For each virus strain/cell type combination, all data (with and without drugs) is fitted simultaneously. In the absence of detailed data on drug effectiveness in these cell types, we make the simplifying assumption that both drugs are 100% effective. Namely, Camostat is assumed to completely inhibit TMPRSS2-dependent pathways (we set $\beta_T = 0$). While Camostat also inhibits other serine proteases, TMPRSS2 is the main serine protease involved in SARS-CoV-2 virus entry, and because the activation of S2′ in TMPRSS2-independent pathways probably occurs by cathepsin proteases rather than serine proteases, for simplicity we assume that Camostat does not affect TMPRSS2-independent pathways. Amphotericin B is assumed to completely remove endosomal restriction (we set $f_E = f_T = 0$).

2.2.3. Inferential framework

We calibrated the models to the observed data in a Bayesian inferential framework using Markov chain Monte Carlo (MCMC) methods. In the results, we reported the median and 95% credible interval (CrI) of the parameter estimates. Full details of the model fitting algorithms are provided in the electronic supplementary material.

All code is available at https://github.com/ada-w-yan/deltaomicronmodelling.

3. Results

3.1. Data description

Figure 4 summarizes the study data. In control wells with no drug, temporal trends in viral growth varied both between strains and cell type. In hNECs, Omicron grew more rapidly than Delta, with viral load peaking by 1 day post infection (p.i.) for Omicron, compared with 2 days p.i. for Delta. However, despite this initial growth advantage, viral load was higher for Delta compared with Omicron at 3 days p.i.. In Calu-3 cells,

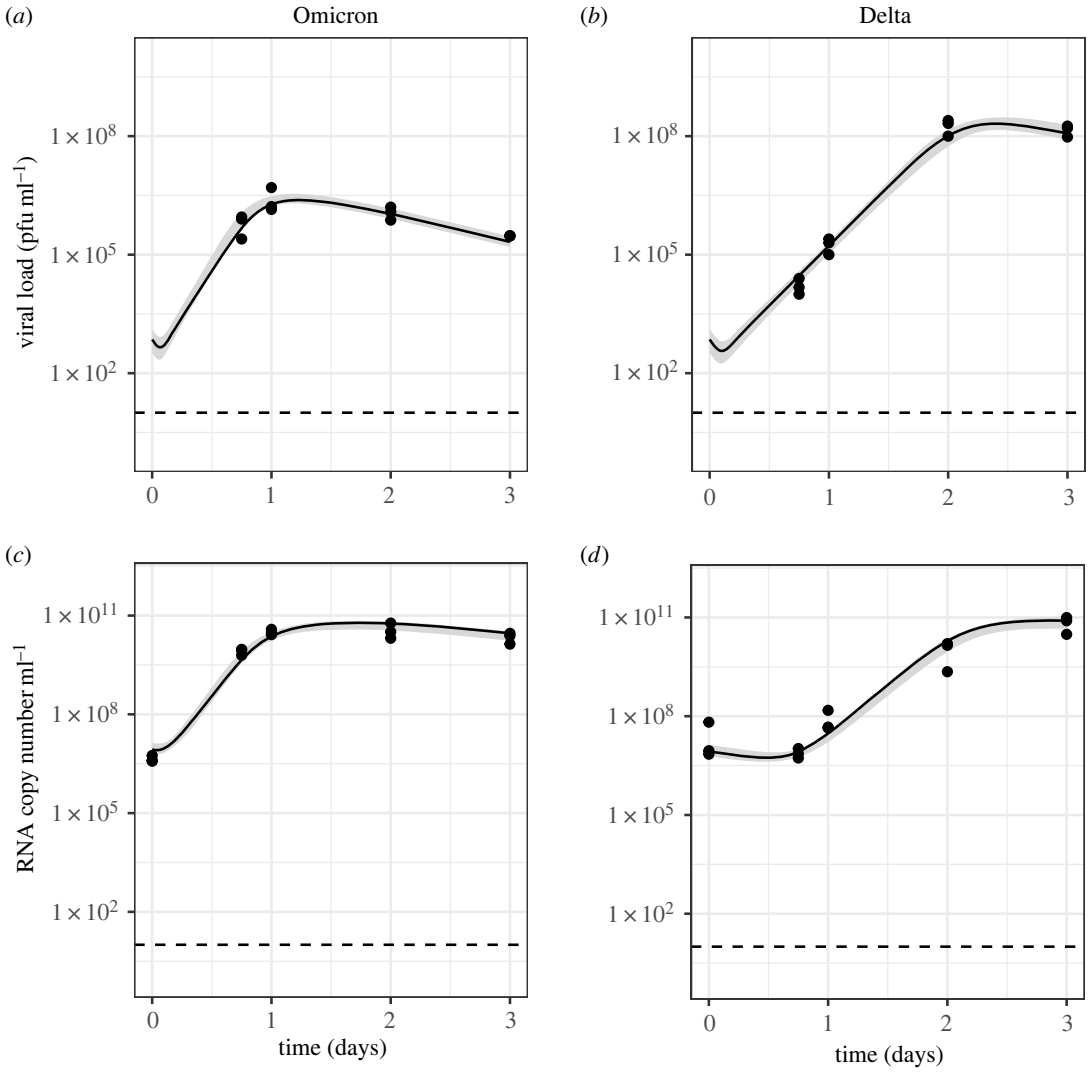

Figure 5. Model 1 fits to data from hNECs without drugs. Dots show the data, black lines show the maximum-likelihood fit, shaded areas show the 95% CrI and dotted lines show the limit of detection.

the peak in viral load was observed 2–3 days p.i. for both Omicron and Delta. In contrast with hNECs where the strain corresponding to the highest viral load was dependent on measurement time, infectious and non-infectious viral load was higher for Delta than Omicron across all time points for Calu-3 cells.

In the presence of the drug Camostat which inhibits serine proteases, and thus TMPRSS2-dependent pathways, replication of Delta was severely inhibited in hNECs with no detectable increase in virus throughout the course of the experiment. By contrast, Omicron successfully replicated in hNECs in the presence of Camostat, albeit at a slower rate than in untreated wells. However, similar levels of viral load were obtained by 2–3 days p.i. in both the presence and absence of Camostat. For both strains, the presence of Amphotericin B had little impact on viral load dynamics in hNECs. In Calu-3 cells, infectious virus was not detected at any point for either Omicron or Delta in the presence of Camostat. In the presence of the drug Amphotericin B which is described as specifically inhibiting endosomal restriction [22,39], Omicron infectious viral titres were consistently higher than in control wells, until 3 days p.i. when titres became similar. Delta geometric mean infectious viral titres were similar with and without Amphotericin B.

Experiments with both drugs combined were only performed for Calu-3 cells. For both virus strains, the infectious viral load was below the limit of detection in the presence of Camostat only. Adding Amphotericin B raised the infectious viral load to above the limit of detection for all replicates for Omicron, but only for some replicates for Delta (figure 4).

3.2. Viral fitness

3.2.1. Model 1

For both Omicron and Delta, the simple model (Model 1) captured the viral dynamics observed in control wells of hNECs and Calu-3 cells (figures 5 and 6). For hNECs, we estimated a higher target cell infection rate β for Omicron relative to Delta (2.13×10^{-05} (95% CrI: 1.54×10^{-05}, 3.07×10^{-05}) cell (pfu ml^{-1})$^{-1}$ day^{-1} for Omicron, 8.89×10^{-08} (95% CrI: 5.91×10^{-08}, 1.28×10^{-07}) cell (pfu ml^{-1})$^{-1}$ day^{-1} for Delta), but a lower infectious virus production rate ω_{Inf} for Omicron relative to Delta ($4.07 \times 10^{+03}$ (95% CrI: $3.13 \times 10^{+03}$, $5.50 \times 10^{+03}$) pfu ml^{-1} cell^{-1} day^{-1} for Omicron, $3.42 \times 10^{+05}$ (95% CrI: $2.41 \times 10^{+05}$, $5.04 \times 10^{+04}$ pfu ml cell^{-1} day^{-1} for Delta). Hence, we estimate an approximately 200-fold increase in infectivity and 100-fold decrease in infectious virus production when comparing Omicron with Delta in hNECs. All estimated parameters are presented in electronic supplementary material, table S2. These results suggest an approximately 1.5-fold difference in the growth rate between these strains in hNECs, with a growth rate of 11.61 day^{-1} (95% CrI: 10.43, 12.99) for Omicron and 6.87 day^{-1} (95% CrI: 6.33, 7.50) for Delta. Furthermore, we

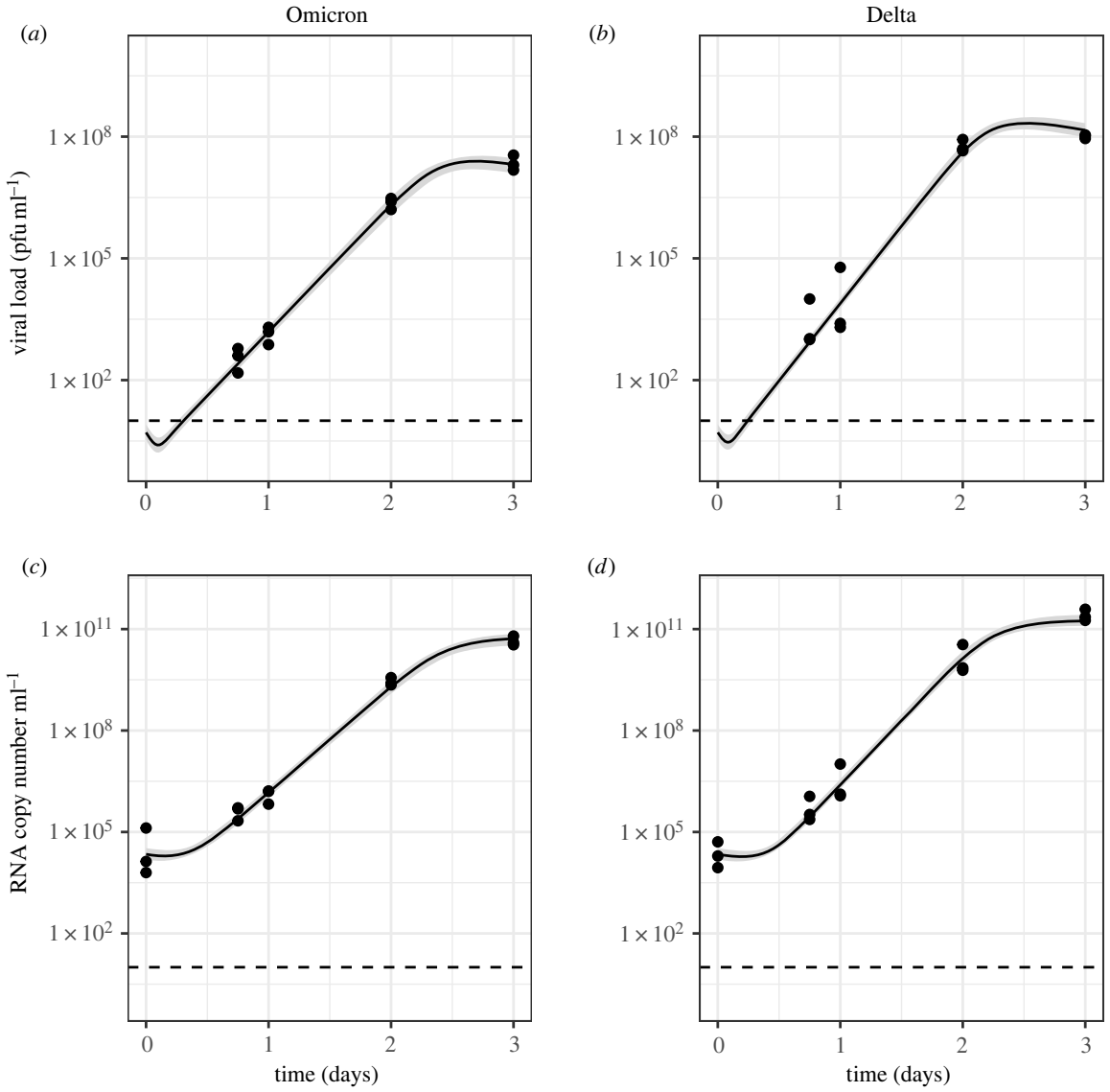

Figure 6. Model 1 fits to data from Calu-3 cells without drugs. Dots show the data, black lines show the maximum-likelihood fit, shaded areas show the 95% CrI and dotted lines show the limit of detection.

estimated a higher basic reproduction number (R_0) for Omicron (65.04 (95% CrI: 51.94, 82.71)) compared with Delta (23.13 (95% CrI: 19.91, 27.23)), thereby suggesting an overall increase in viral fitness of Omicron relative to Delta in hNECs.

For Calu-3 cells, we estimated a higher target cell infection rate for Omicron than Delta (9.23×10^{-07} (95% CrI: 6.17×10^{-07}, 1.36×10^{-06}) cell (pfu ml^{-1})$^{-1}$ day^{-1} for Omicron, 1.42×10^{-07} (95% CrI: 9.80×10^{-08}, 2.05×10^{-07}) cell (pfu ml^{-1})$^{-1}$ day^{-1} for Delta) and lower infectious virus production rate for Omicron than Delta ($4.13 \times 10^{+02}$ (95% CrI: $2.85 \times 10^{+02}$, $6.07 \times 10^{+02}$) cell (pfu ml^{-1})$^{-1}$ day^{-1} for Omicron, $3.73 \times 10^{+03}$ (95% CrI: $2.67 \times 10^{+03}$, $5.32 \times 10^{+03}$) cell (pfu ml^{-1})$^{-1}$ day^{-1} for Delta). In contrast with hNECs, our results indicate an overall increase in viral fitness of Delta relative to Omicron in Calu-3 cells as we estimated a higher basic reproduction number of Delta (36.67 (95% CrI: 33.69, 39.81)) compared with Omicron (24.23 (95% CrI: 22.14, 26.70)) in this cell type. In addition, we estimated a larger growth rate of Delta relative to Omicron in Calu-3 cells, with a growth rate of 8.78 day^{-1} (95% CrI: 8.40, 9.15) for Delta compared with 7.25 day^{-1} (95% CrI: 6.86, 7.60) for Omicron (for details see electronic supplementary material, table S2).

For both cell types, the target cell infection rate (β), which is positively correlated with the probability of a virion successfully infecting a cell, was higher for Omicron than Delta. The infectious virus production rate (ω_{Inf}), which is directly proportional to the burst size (the total number of infectious virions produced by one infected cell), was higher for Delta than Omicron. However, the magnitude of each of these differences meant that the basic reproduction number and growth rate, which are both functions of the target cell infection rate and the infectious virus production rate (see electronic supplementary material, methods), were higher for Omicron in hNECs, but higher for Delta in Calu-3 cells (electronic supplementary material, table S2).

3.2.2. Model 2

When fitting Model 2 to the data, we found the same qualitative result that Omicron's R_0 is higher than Delta's in hNECs, but lower in Calu-3 cells (figures 7 and 8). In hNECs, R_0 for Omicron was estimated to be 106.59 (95% CrI: 85.92, 134.72), while for Delta it was estimated to be 21.61 (95% CrI: 18.97, 25.30). In Calu-3 cells, R_0 for Omicron was estimated to be 16.53 (95% CrI: 15.15, 17.99), and for Delta was estimated to be 27.87 (95% CrI: 25.60, 30.34). R_0 estimates were comparable between Models 1 and 2, except for Omicron in hNECs, where the R_0 estimates obtained with Model 2 were higher. This discrepancy occurred because Model 2 predicts that Omicron can use both

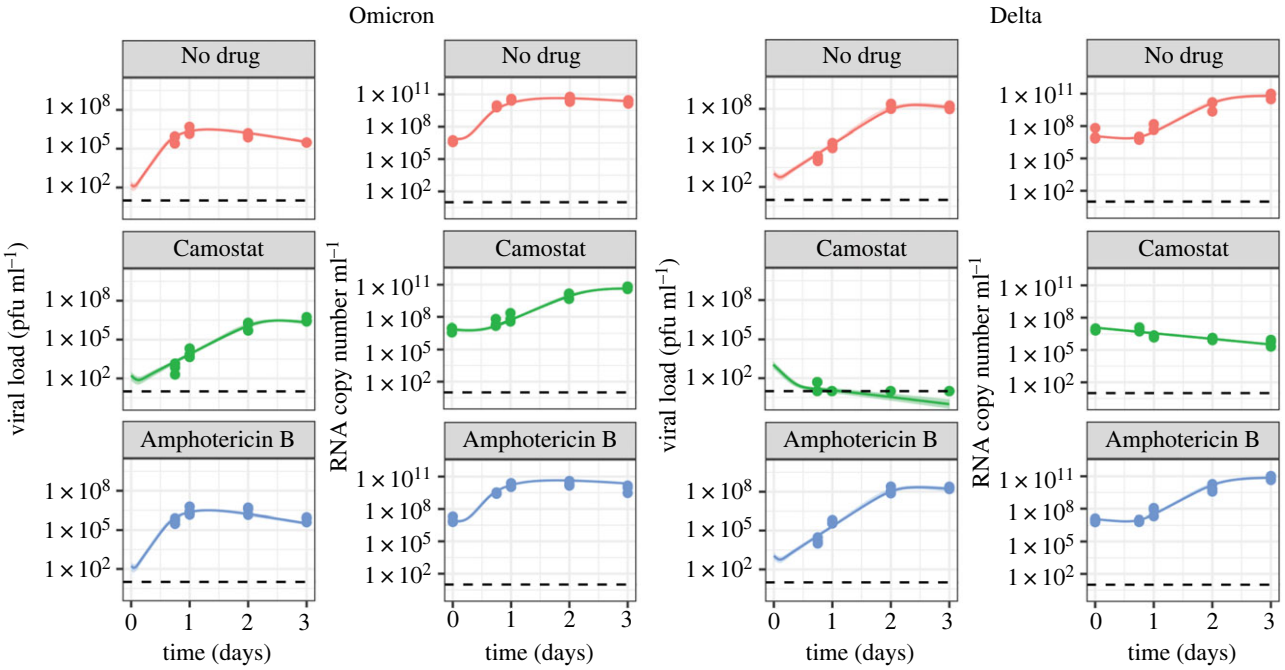

Figure 7. Model 2 fits to data from hNECs with and without drugs. Dots show the data, black lines show the maximum-likelihood fit, shaded areas show the 95% CrI and dotted lines show the limit of detection. Markers on the lines represent measurements below the limit of detection.

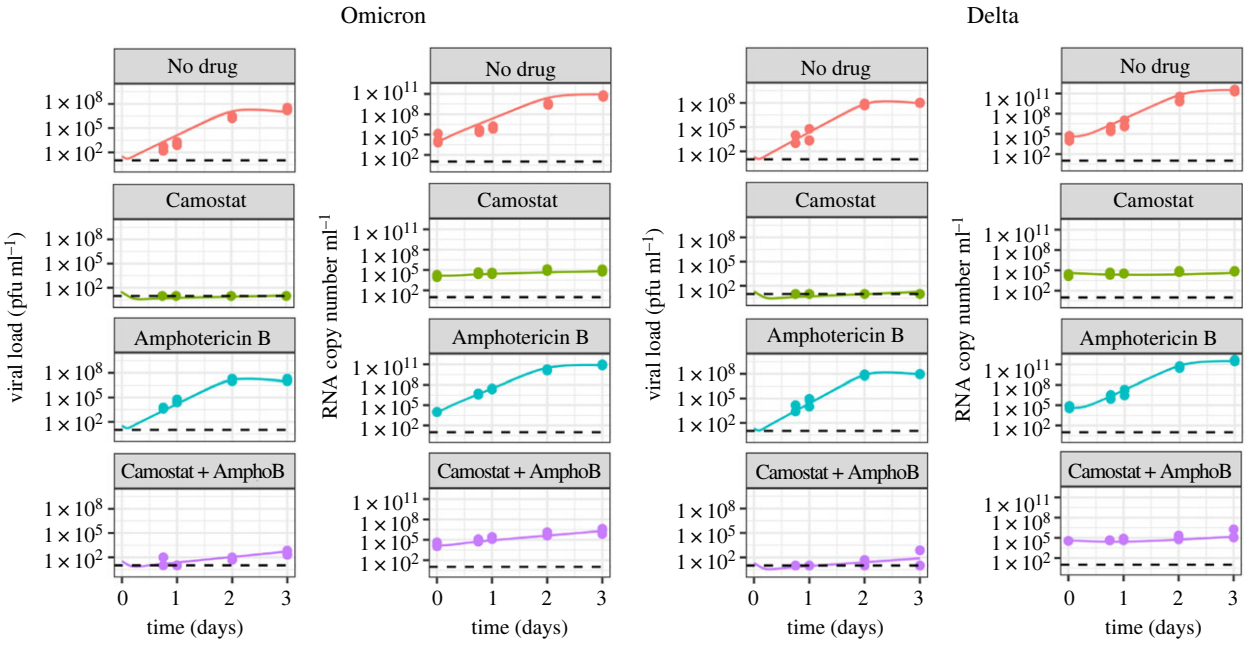

Figure 8. Model 2 fits to data from Calu-3 cells with and without drugs. Dots show the data, black lines show the maximum-likelihood fit, shaded areas show the 95% CrI and dotted lines show the limit of detection. Markers on the lines represent measurements below the limit of detection.

TMPRSS2-dependent and TMPRSS2-independent pathways in hNECs (see next section), whereas for all other strain and cell combinations, only TMPRSS2-dependent pathways are active. When only TMPRSS2-dependent pathways are active, then in the absence of drug, Models 1 and 2 are the same. All parameter estimates are presented in electronic supplementary material, table S2.

3.3. Role of cell entry pathways

As Camostat inhibits serine proteases including TMPRSS2, Camostat-sensitive viruses must be able to use TMPRSS2-independent pathways for cell entry; thus, the fit of Model 2 to the data in the presence of Camostat provides information on the role of cell entry pathways. We found that in hNECs, Omicron was able to use both TMPRSS2-dependent and TMPRSS2-independent pathways. The median estimates of R_{0T} and R_{0E} were 92.13 (95% CrI: 72.95, 118.27) and 15.44 (95% CrI 12.86, 18.52) respectively (electronic supplementary material, table S3). On the other hand, in hNECs, Delta was unable to effectively use TMPRSS2-independent pathways, as $R_{0E} < 1$ (median 0.15, 95% CrI: (0.07, 0.30)). In Calu-3 cells, neither virus was able to use TMPRRS2-independent pathways effectively. R_{0E} was estimated to be slightly greater than 1 for both Omicron (median 1.34 (95% CrI: 1.14, 1.55)) and Delta (median 1.71 (95% CrI: 1.47, 1.98)) but these small values of

R_0 are insufficient for the viral load to exceed the limit of detection during the time course of the experiment (figure 8, Camostat panels). Note that for Omicron in hNECs, the estimate for R_{0T} is comparable to the overall R_0 for Model 1. This is because the increase in viral load due to TMPRSS2-dependent pathways is much faster than through TMPRSS2-independent pathway, so the TMPRSS2-dependent pathway is the main contributor to the initial exponential increase, from which Model 1 estimates R_0.

It has been suggested that Omicron's use of TMPRRS2-independent pathways explains its fitness advantage over Delta [13,14,17]. However, even the TMPRSS2-specific basic reproduction number is higher for Omicron than Delta in hNECs, with a median R_{0T} equal to 92.13 (95% CrI: 72.95, 118.27) for Omicron compared with 21.46 (95% CrI:18.89, 25.05) for Delta. In fact, R_{0T} alone for Omicron is greater than the overall R_0 for Delta. Therefore, it is primarily Omicron's more efficient use of TMPRSS2-dependent pathways, rather than its utilization of TMPRSS2-independent pathways, which gives it a fitness advantage over Delta in hNECs.

3.4. Role of endosomal restriction

As Amphotericin B inhibits restrictions to virus entry imposed by endosomal restriction factors, the fit of Model 2 to the Amphotericin B data provides information on the role of endosomal restriction factors in shaping the viral dynamics observed. The parameters f_E and f_T capture the degree of inhibition of TMPRSS2-independent and TMPRSS2-dependent pathways by endosomal restriction factors respectively, and Amphotericin B is assumed to set these parameters to 0. Comparing across cell types, inhibition by endosomal restriction factors was higher in Calu-3 cells than hNECs across all strains and pathways (higher values of f_E and f_T for Calu-3 cells compared with hNEC cells in electronic supplementary material, table S2), with the exception of TMPRSS2-independent pathways for Delta, where f_E could not be estimated precisely. Inhibition was similar for both Omicron and Delta in hNECs, but Omicron was more inhibited by endosomal restriction factors than Delta in Calu-3 cells for both pathways (higher values of f_E and f_T for Omicron than Delta in Calu-3 cells in electronic supplementary material, table S2). Comparing across pathways, f_E and f_T were similar for each virus strain in hNECs, but in Calu-3 cells, f_E was higher than f_T for both virus strains, suggesting more inhibition of TMPRSS2-independent pathways than of TMPRSS2-dependent pathways.

Given that TMPRSS2-independent pathways are susceptible to inhibition by endosomal restriction factors, and that previous variants were not able to use endosomal restriction pathways, one may hypothesize that Omicron has overcome endosomal restriction in hNECs, and that TMPRSS2-independent pathways would also be accessible by other virus–cell combinations if endosomal restriction were lifted. However, we predict that even if endosomal restriction is lifted for the three other virus-cell combinations (as per the Amphotericin B experiments) R_{0EX} remains low. This suggests that other factors contribute to Omicron's increased use of TMPRSS2-independent pathways in hNECs. We predict that in the absence of endosomal restriction factors, Omicron would still have a higher overall basic reproduction number and growth rate than Delta in hNECs, but these quantities would be similar between variants in Calu-3 cells (R_{0X} in electronic supplementary material, table S3 and r_X in electronic supplementary material, table S6).

3.5. Sensitivity of results to the values of fixed parameters

A caveat of the above results is that we have fixed the values of several parameters: the length of the eclipse phase, the infected cell decay rate and the infectious virus decay rate. The eclipse phase in this model reflects the speed of viral replication with the cell. To date, studies which have measured the duration of the eclipse phase in the SARS-CoV-2 viral life cycle have used viruses which enter target cells through TMPRSS2-dependent pathways only [48,49]. Thus, the duration of the eclipse phase for TMPRSS2-independent pathways is unclear and our knowledge of this component of the viral life cycle is limited. To address this, we conducted a sensitivity analysis around the duration of the eclipse phase. In Model 1, τ was set to 6, 4, or 2 day^{-1}. In Model 2, τ_T was set to 6, 4 or 2 day^{-1}, and τ_E was set to 4, 2 or 1 day^{-1}. We found that for Model 1, regardless of the duration of the eclipse phase assumed—as long as it was the same between strains—Omicron had a higher R_0 than Delta in hNECs, and Delta had a higher R_0 than Omicron in Calu-3 cells (electronic supplementary material, table S4). Also, all estimated R_0 values decreased as the duration of the eclipse phase decreased, as expected theoretically. This is because if, at the start of infection, cells start producing virus sooner due to a short eclipse phase, then each individual infected cell needs to lead to fewer secondary infections to reproduce the dynamics observed. In detail, shortening the assumed eclipse phase shortens the generation time. The growth rate is directly related to the slope of the viral load curve and thus its estimated value is insensitive to changes in the assumed eclipse phase; however, the same growth rate can be achieved using a small R_0 and a short generation time, or a large R_0 and a long generation time. Decreasing the assumed generation time thus decreases the estimated value of R_0. Similarly, for Model 2, we found that regardless of the values of τ_E and τ_T, as long as these were assumed to be the same between strains, Omicron had a higher R_0 than Delta in hNECs, and Delta had a higher R_0 than Omicron in Calu-3 cells; only Omicron in hNECs used TMPRSS2-independent pathways efficiently; and endosomal restriction only had a significant effect in Calu-3 cells (electronic supplementary material, table S5). However, allowing the duration of the eclipse phase to be different between strains, no longer allows us to draw conclusions about whether R_0 is greater for Omicron or Delta (electronic supplementary material, tables S3 and S5). On the other hand, estimates of the growth rate r only varied slightly with the assumed duration of the eclipse phase for both models (electronic supplementary material, tables S4 and S6).

The infected cell decay rate is inversely proportional to its lifetime, and has not been measured directly; its value has been estimated using within-host mathematical models [25], but this parameter is known to be unidentifiable given viral load data alone [50]. We therefore conducted a sensitivity analysis by setting δ to 0.1, 0.85, 1.7, 3.4 and 10 day^{-1} (electronic supplementary material, tables S7–S10). For Model 1, similarly to when changing the duration of the eclipse phase, the main conclusions of this study remained the same, with Omicron having a higher R_0 than Delta in

hNECs and Delta have a higher R_0 than Omicron in Calu-3 cells (electronic supplementary material, table S7 and S8). For Model 2, for $\delta = 0.1$ day^{-1}, we estimated a median R_{0E} of 9.03 (95% CrI: 6.86, 11.63) for Omicron and 13.61 (95% CrI: 10.50, 17.15) for Delta in Calu-3 cells (electronic supplementary material, table S9). This might suggest that TMPRSS2-independent pathways were efficiently used in Calu-3 cells; however, the corresponding median growth rates were still low ($r_E = 0.63$ (95% CrI: 0.48, 0.80) for Omicron, 0.92 (95% CrI: 0.73, 1.11) for Delta (electronic supplementary material, table S10). $\delta = 0.1$ day^{-1} corresponds to a generation time of 10.3 days, so although each initial infectious virion results in 10 secondary infectious virions on average, the timescale on which those virions would be produced would be beyond the resolution time of an acute infection *in vivo*. Hence, this would still indicate $R_{0E} > 1$. As with changing the eclipse phase, comparisons between growth rates for Model 2 remained robust whether δ was the same or different between variants and cell types, but this was not the case for comparisons between reproduction numbers.

The infectious virus decay rate has been measured directly [51,52], but there is evidence that it differs between variants [53]. We therefore conducted a sensitivity analysis, setting κ_{Inf} to 1.2, 5, 10, 20 or 100 day^{-1} (electronic supplementary material, tables S11-S14). For Model 1, the main conclusions remained the same. For Model 2, comparisons between growth rates remained robust whether κ_{Inf} was the same or different between variants and cell types, but this was not the case for comparisons between reproduction numbers.

4. Discussion

By fitting a simple within-host model to viral kinetics data for Omicron and Delta in hNECs and Calu-3 cells, we found that Omicron has a fitness advantage over Delta in hNECs, but Delta has a fitness advantage over Omicron in Calu-3 cells, as measured by both the growth rate and basic reproduction number of the virus. These findings are consistent with previously published studies showing faster replication of Omicron compared with Delta in human nasal epithelial cells [14,15], and faster replication of Delta compared with Omicron in the *ex vivo* explant cultures of human lungs [13] and Calu-3 cells [54].

We estimated that Omicron had a higher rate of infection β in both cell types, which could be linked to increased ACE2 binding affinity, probably due to mutations in the spike protein. Evidence is mixed as to whether Omicron has a higher ACE2 binding affinity than Delta. Cameroni *et al*. [55] found that Omicron has a higher human ACE2 binding affinity than Delta, but Mannar *et al*. [56] found that ACE2 binding affinity is similar for Omicron and Delta, though higher than the ancestral strain. On the other hand, Zhang *et al*. [57] found that the Omicron spike protein required a higher level of ACE2 than Delta for efficient membrane fusion. We also estimated that Omicron had a lower rate of infectious virus production ω_{Inf} than Delta for both cell types. Changes to the rate of viral production could be due to mutations in either spike or non-spike proteins. The basic reproduction number is positively correlated with both the rate of infection β and the rate of infectious virus production ω_{Inf} in our models. In hNECs, the increase in the rate of infection β for Omicron was greater than the decrease in infectious virus production ω_{Inf}, resulting in a larger basic reproduction number and growth rate for Omicron compared with Delta; the converse was true in Calu-3 cells.

Previous studies have proposed that TMPRSS2-independent pathways, which are only available to Omicron, are responsible for its faster growth in hNECs. Our study found that Omicron can use TMPRSS2-independent pathways in hNECs, consistent with the previous studies. However, the growth rate and basic reproduction number for TMPRSS2-independent pathways was low and insufficient to explain the overall fitness advantage for Omicron over Delta in hNECs. On the other hand, the growth rate and basic reproduction number for TMPRSS2-dependent pathways was also higher for Omicron than Delta in hNECs and was sufficient to explain the overall fitness advantage. Evidence for the continued importance of TMPRSS2-dependent pathways for Omicron was provided by a study by Metzdorf *et al*. [58], which found that the growth of Omicron in the nose and lung was attenuated in TMPRSS2 knockout mice. In Calu-3 cells, neither Omicron nor Delta can use TMPRSS2-independent pathways, thereby providing further insight into how these viruses use different pathways to enter target cells.

We estimated the degree of inhibition in viral growth imposed by endosomal restriction factors by fitting our model to data where the cells were treated with Amphotericin B, as Amphotericin B inhibits the action of endosomal restriction factors. The main hypotheses tested were (i) whether Omicron was able to evade endosomal restriction in hNECs; (ii) whether this evasion enabled Omicron to use TMPRSS2-independent pathways; and (iii) whether this was responsible for Omicron's growth advantage. We found that the fitness of Delta in hNECs without endosomal restriction, as measured by the basic reproduction number R_{0X} and the growth rate r_X, was still lower than that of Omicron in hNECs with endosomal restriction. Hence, reduced endosomal restriction alone does not explain Omicron's fitness advantage in hNECs. Although we were able to quantify the degree of inhibition by endosomal restriction factors for both pathways for Omicron in hNECs, we were unable to for Delta, as doing so requires either the infectious viral load to be above the limit of detection in the presence of Camostat (as was the case for Omicron in hNECs), or requires data on viral growth in the presence of both drugs (as was the case in Calu-3 cells). Hence, we were unable to make a direct comparison at a pathway-specific level between Omicron and Delta in hNECs. In Calu-3 cells, we found that Omicron was more inhibited by endosomal restriction factors than Delta, for both TMPRSS2-dependent or TMPRSS2-independent pathways.

Human nasal and lung cells were used in the experiments to recapitulate replication in the nose and lung. For nasal cells, primary differentiated nasal airway epithelial cells cultured at an air–liquid interface were used. These cells represent the major cell types in the nose, and have previously been used to compare the growth of SARS-CoV-2 variants [18]. For lung cells, the immortalized Calu-3 cell line was used as Calu-3 cells express both ACE2 and TMPRSS2 proteins, and thus are amenable to SARS-CoV-2 infection. They have been used to test antivirals against SARS-CoV-2 [19] and compare growth kinetics between variants [59]. However, they do not represent the range of cell types available in the lower respiratory tract, and so future experiments could use primary differentiated

human lung cells (e.g. [60]); however, not all such cultures can be efficiently infected with SARS-CoV-2 to comparable titres as within the respiratory tract [61], so *ex vivo* lung cultures may be another alternative [13].

The model has several limitations. First, we fixed the infected cell death rate, the rate at which viruses lose infectivity, the RNA degradation rate, and the duration of eclipse phases, according to values from the literature. It is currently unclear whether the duration of the eclipse phase differs between variants. Studies have shown that Omicron survives for longer on surfaces than the ancestral strain [62] and Delta [53], so it is plausible that extracellular virus may also differ in stability in our experiments. Moreover, fixing the parameters using values from previous studies may underestimate the uncertainty in the reproduction number and growth rate. To test this, we conducted a sensitivity analysis where the model was fitted assuming different lengths of the eclipse phase, infected cell decay rates, and infectious virus decay rates. This sensitivity analysis showed that, if the values of these three parameters were assumed to be the same between Omicron and Delta, the trends and relationships in R_0 and the growth rate estimates r between Omicron and Delta (for example, that Omicron has a higher R_0 and growth rate estimate r than Delta in hNECs) remained unchanged. Allowing any of these three parameters to be different between strains, no longer allows us to draw conclusions about whether R_0 is greater for Omicron or Delta (electronic supplementary material, tables S3 and S5), but the differences in r are robust. This result reflects the finding that if the eclipse phase is allowed to vary, the growth rate r is identifiable but R_0 is not. Future studies could measure the duration of the eclipse phase for each cell type and virus strain using single-cycle growth kinetics experiments; make the infected cell lifetime identifiable by measuring the number of infected cells over time in addition to the viral load; and measure intracellular RNA and the infectious virus decay rate for each variant.

Another limitation of the model is that it assumes 100% effectiveness for both drugs. Assuming 100% effectiveness of Camostat means interpreting all remaining viral growth as due to TMPRSS2-independent pathways, so if the drug is less than 100% effective, the contribution of TMPRSS2-independent pathways will be overestimated. Assuming 100% effectiveness of Amphotericin B means interpreting viral growth in the presence of Amphotericin B as the viral growth in the complete absence of endosomal restriction. If the drug were less than 100% effective, the viral load in the complete absence of endosomal restriction could be higher than that suggested by the data, so the effect of endosomal restriction would be underestimated.

An additional limitation is that the structure of the model is such that the initial growth rate is independent of the inoculum size. It is plausible that differences in growth rate between hNECs and Calu-3 cells observed in the experiments were partly due to the differing inoculum sizes used, as a higher inoculum could, for example, trigger endosomal restriction factors more quickly—an effect which was not modelled. A higher MOI was used for hNECs as a lower MOI did not always successfully infect these primary cells; repeating the Calu-3 experiments at the same higher MOI would strengthen confidence in our comparison between cell types. We also did not consider the spatial spread of the virus. While an agent-based model could be developed to explore the spatial dynamics of virus in cell culture, fitting such a model would require much more detailed experimental data, which unfortunately was not available for this study.

However, the models developed in this study can inform future studies using more complex models. Models capturing more immune components and how the virus spreads within the host are useful for understanding contributors to disease severity and the effects of antivirals [38–40], but because they have many parameters, it is often difficult to determine their values by fitting them to data. This study can help parametrize these models.

The models developed in this study can be applied to different SARS-CoV-2 virus strains to help enhance our understanding of transmission potential of new strains as the virus continues to evolve. While between-strain differences in the speed of viral replication is typically assessed by comparing viral titre measurements at individual time points, adopting a mathematical modelling approach using longitudinal time points enables us to estimate key characteristics of different strains such as the growth rate and viral fitness, thus providing a deeper insight into the factors shaping observed differences in viral dynamics at the individual and population level.

Ethics. This work did not require ethical approval from a human subject or animal welfare committee.

Data accessibility. All data are available at https://github.com/ada-w-yan/deltaomicronmodelling.

The data are provided in electronic supplementary material [63].

Authors' contributions. C.P.M.: conceptualization, formal analysis, investigation, methodology, writing—original draft, writing—review and editing; A.W.C.Y.: conceptualization, formal analysis, investigation, methodology, software, visualization, writing—original draft, writing—review and editing; J.C.B.: data curation, investigation, writing—review and editing; K.S.: data curation, investigation, writing—review and editing; T.P.P.: investigation, writing—review and editing; W.S.B.: conceptualization, funding acquisition, investigation, supervision, writing—review and editing; I.D.: conceptualization, funding acquisition, investigation, methodology, supervision, writing—review and editing.

All authors gave final approval for publication and agreed to be held accountable for the work performed therein.

Conflict of interest declaration. The authors declare no competing financial interests.

Funding. C.P.M. and I.D. acknowledge funding from the MRC Centre for Global Infectious Disease Analysis (reference MR/R015600/1), jointly funded by the UK Medical Research Council (MRC) and the UK Foreign, Commonwealth & Development Office (FCDO), under the MRC/FCDO Concordat agreement and is also part of the EDCTP2 programme supported by the European Union. A.W.C.Y. acknowledges funding from an Imperial College Research Fellowship. I.D. acknowledges funding by the Wellcome Trust and Royal Society (grant no. 213494/Z/18/Z). This study was conducted as part of G2P-UK National Virology consortium funded by MRC/UKRI (MR/W005611/1). For the purpose of open access, the authors have applied a CC BY public copyright licence to any Author Accepted Manuscript version arising from this submission.

References

1. WHO. 2021 *Classification of Omicron (B.1.1.529): SARS-CoV-2 Variant of Concern*. WHO. See https://www.who.int/news/item/26-11-2021-classification-of-omicron-(b.1.1.529)-sars-cov-2-variant-of-concern.

2. GISAID. 2022 *GISAID-hCov19 Variants*. GISAID. See https://gisaid.org/hcov19-variants/.

3. WHO. 2021 *Tracking SARS-CoV-2 variants*. WHO. See https://www.who.int/activities/tracking-SARS-CoV-2-variants.
4. Viana R *et al.* 2022 Rapid epidemic expansion of the SARS-CoV-2 Omicron variant in southern Africa. *Nature* **603**, 679–686. (doi:10.1038/s41586-022-04411-y)
5. Cele S *et al.* 2022 Omicron extensively but incompletely escapes Pfizer BNT162b2 neutralization. *Nature* **602**, 654–656. (doi:10.1038/s41586-021-04387-1)
6. Planas D *et al.* 2022 Considerable escape of SARS-CoV-2 Omicron to antibody neutralization. *Nature* **602**, 671–675. (doi:10.1038/s41586-021-04389-z)
7. Cao Y *et al.* 2022 Omicron escapes the majority of existing SARS-CoV-2 neutralizing antibodies. *Nature* **602**, 657–663. (doi:10.1038/s41586-021-04385-3)
8. Dejnirattisai W *et al.* 2022 SARS-CoV-2 Omicron-B.1.1.529 leads to widespread escape from neutralizing antibody responses. *Cell* **185**, 467–484.e15. (doi:10.1016/j.cell.2021.12.046)
9. Andrews N *et al.* 2022 Covid-19 vaccine effectiveness against the Omicron (B.1.1.529) Variant. *N. Engl. J. Med.* **386**, 1532–1546. (doi:10.1056/NEJMoa2119451)
10. Nyberg T *et al.* 2022 Comparative analysis of the risks of hospitalisation and death associated with SARS-CoV-2 Omicron (B.1.1.529) and Delta (B.1.617.2) variants in England: a cohort study. *Lancet* **399**, 1303–1312. (doi:10.1016/S0140-6736(22)00462-7)
11. Wolter N *et al.* 2022 Early assessment of the clinical severity of the SARS-CoV-2 Omicron variant in South Africa: a data linkage study. *Lancet* **399**, 437–446. (doi:10.1016/S0140-6736(22)00017-4)
12. Mefsin YM *et al.* 2022 Epidemiology of infections with SARS-CoV-2 Omicron BA.2 Variant, Hong Kong, January–March 2022. *Emerg. Infect. Dis.* **28**, 1856–1858. (doi:10.3201/eid2809.220613)
13. Hui KPYY *et al.* 2022 SARS-CoV-2 Omicron variant replication in human bronchus and lung ex vivo. *Nature* **603**, 715–720. (doi:10.1038/s41586-022-04479-6)
14. Willett BJ *et al.* 2022 SARS-CoV-2 Omicron is an immune escape variant with an altered cell entry pathway. *Nat. Microbiol.* **7**, 1161–1179. (doi:10.1038/s41564-022-01143-7)
15. Barut GT *et al.* 2022 The spike gene is a major determinant for the SARS-CoV-2 Omicron-BA.1 phenotype. *Nat. Commun.* **13**, 1–14. (doi:10.1038/s41467-022-33632-y)
16. Lyngse FP *et al.* 2022 Household transmission of the SARS-CoV-2 Omicron variant in Denmark. *Nat. Commun.* **13**, 5573. (doi:10.1038/s41467-022-33328-3)
17. Meng B *et al.* 2022 Altered TMPRSS2 usage by SARS-CoV-2 Omicron impacts infectivity and fusogenicity. *Nature* **603**, 706–714. (doi:10.1038/s41586-022-04474-x)
18. Suzuki R *et al.* 2022 Attenuated fusogenicity and pathogenicity of SARS-CoV-2 Omicron variant. *Nature* **603**, 700–705. (doi:10.1038/s41586-022-04462-1)
19. Hoffmann M *et al.* 2020 SARS-CoV-2 cell entry depends on ACE2 and TMPRSS2 and is blocked by a clinically proven protease inhibitor. *Cell* **181**, 271–280.e8. (doi:10.1016/j.cell.2020.02.052)
20. Peacock TP *et al*. 2022 The altered entry pathway and antigenic distance of the SARS-CoV-2 Omicron variant map to separate domains of spike protein. *bioRxiv*. 2021.12.31.474653. (doi:10.1101/2021.12.31.474653)
21. Winstone H *et al.* 2021 The polybasic cleavage site in SARS-CoV-2 spike modulates viral sensitivity to Type I interferon and IFITM2. *J. Virol.* **95**, e02422-20. (doi:10.1128/JVI.02422-20)
22. Peacock TP *et al.* 2021 The furin cleavage site in the SARS-CoV-2 spike protein is required for transmission in ferrets. *Nat. Microbiol.* **6**, 899–909. (doi:10.1038/s41564-021-00908-w)
23. Khan H *et al.* 2021 TMPRSS2 promotes SARS-CoV-2 evasion from NCOA7-mediated restriction. *PLoS Pathog.* **17**, e1009820. (doi:10.1371/journal.ppat.1009820)
24. Challenger JD *et al.* 2022 Modelling upper respiratory viral load dynamics of SARS-CoV-2. *BMC Med.* **20**, 1–20. (doi:10.1186/s12916-021-02220-0)
25. Ke R, Zitzmann C, Ho DD, Ribeiro RM, Perelson AS. 2021 In vivo kinetics of SARS-CoV-2 infection and its relationship with a person's infectiousness. *Proc. Natl Acad. Sci. USA* **118**, e2111477118. (doi:10.1073/pnas.2111477118)
26. Néant N *et al.* 2021 Modeling SARS-CoV-2 viral kinetics and association with mortality in hospitalized patients from the French COVID cohort. *Proc. Natl Acad. Sci. USA* **118**, e2017962118. (doi:10.1073/pnas.2017962118)
27. Kim KS *et al.* 2021 A quantitative model used to compare within-host SARS-CoV-2, MERS-CoV, and SARS-CoV dynamics provides insights into the pathogenesis and treatment of SARS-CoV-2. *PLoS Biol.* **19**, e3001128. (doi:10.1371/journal.pbio.3001128)
28. Gonçalves A *et al.* 2020 Timing of antiviral treatment initiation is critical to reduce SARS-CoV-2 viral load. *CPT Pharmacometrics Syst. Pharmacol.* **9**, 509–514. (doi:10.1002/psp4.12543)
29. Gonçalves A *et al.* 2021 SARS-CoV-2 viral dynamics in non-human primates. *PLoS Comput. Biol.* **17**, e1008785.
30. Perelson AS, Ke R. 2021 Mechanistic modeling of SARS-CoV-2 and other infectious diseases and the effects of therapeutics. *Clin. Pharmacol. Ther.* **109**, 829–840. (doi:10.1002/cpt.2160)
31. Koelle K *et al*. 2022 Masks do no more than prevent transmission: theory and data undermine the variolation hypothesis. *medRxiv* 2022.06.28.22277028 (doi:10.1101/2022.06.28.22277028)
32. Ito K, Piantham C, Nishiura H. 2022 Relative instantaneous reproduction number of Omicron SARS-CoV-2 variant with respect to the Delta variant in Denmark. *J. Med. Virol.* **94**, 2265–2268. (doi:10.1002/jmv.27560)
33. Lingas G *et al.* 2022 Effect of remdesivir on viral dynamics in COVID-19 hospitalized patients: a modelling analysis of the randomized, controlled, open-label DisCoVeRy trial. *J. Antimicrob. Chemother.* **77**, 1404–1412. (doi:10.1093/jac/dkac048)
34. Goyal A, Cardozo-Ojeda EF, Schiffer JT. 2020 Potency and timing of antiviral therapy as determinants of duration of SARS-CoV-2 shedding and intensity of inflammatory response. *Sci. Adv.* **6**, eabc7112. (doi:10.1126/sciadv.abc7112)
35. Goyal A *et al.* 2021 Slight reduction in SARS-CoV-2 exposure viral load due to masking results in a significant reduction in transmission with widespread implementation. *Sci. Rep.* **11**, 1–12. (doi:10.1038/s41598-021-91338-5)
36. Goyal A, Duke ER, Cardozo-Ojeda EF, Schiffer JT. 2022 Modeling explains prolonged SARS-CoV-2 nasal shedding relative to lung shedding in remdesivir-treated rhesus macaques. *iScience* **25**, 104448. (doi:10.1016/j.isci.2022.104448)
37. Alexandre M *et al.* 2022 Modelling the response to vaccine in nonhuman primates to define SARS-CoV-2 mechanistic correlates of protection. *Elife* **11**, e75427. (doi:10.7554/eLife.75427)
38. Jenner AL *et al.* 2021 COVID-19 virtual patient cohort suggests immune mechanisms driving disease outcomes. *PLoS Pathog.* **17**, e1009753. (doi:10.1371/journal.ppat.1009753)
39. Rowlatt CF *et al*. 2022 Modelling the within-host spread of SARS-CoV-2 infection, and the subsequent immune response, using a hybrid, multiscale, individual-based model. Part I: Macrophages. *bioRxiv*. (doi:10.1101/2022.05.06.490883)
40. Wang, Y. *et al*. 2020 Rapid community-driven development of a SARS-CoV-2 tissue simulator. *bioRxiv* 4, 2020.04.02.019075.
41. Marc A *et al.* 2021 Quantifying the relationship between SARS-CoV-2 viral load and infectiousness. *Elife* **10**, e69302. (doi:10.7554/eLife.69302)
42. Goyal A, Reeves DB, Schiffer JT. 2022 Multi-scale modelling reveals that early super-spreader events are a likely contributor to novel variant predominance. *J. R. Soc. Interface* **19**, 20210811. (doi:10.1098/rsif.2021.0811)
43. Larremore DB *et al.* 2021 Test sensitivity is secondary to frequency and turnaround time for COVID-19 screening. *Sci. Adv.* **7**, eabd5393. (doi:10.1126/sciadv.abd5393)
44. Hay JA *et al.* 2021 Estimating epidemiologic dynamics from cross-sectional viral load distributions. *Science* **373**, eabh0635. (doi:10.1126/science.abj5260)
45. Brass AL *et al.* 2009 The IFITM proteins mediate cellular resistance to influenza A H1N1 virus, West Nile virus, and dengue virus. *Cell* **139**, 1243–1254. (doi:10.1016/j.cell.2009.12.017)
46. Lin TY *et al.* 2013 Amphotericin B increases influenza A virus infection by preventing IFITM3-mediated restriction. *Cell Rep.* **5**, 895–908. (doi:10.1016/j.celrep.2013.10.033)
47. Qian J *et al.* 2015 Primate lentiviruses are differentially inhibited by interferon-induced transmembrane proteins. *Virology* **474**, 10–18. (doi:10.1016/j.virol.2014.10.015)
48. Brahim Belhaouari D *et al.* 2020 The strengths of scanning electron microscopy in deciphering SARS-

CoV-2 infectious cycle. *Front. Microbiol.* **11**, 2014. (doi:10.3389/fmicb.2020.02014)

49. Hou YJ *et al.* 2020 SARS-CoV-2 D614G variant exhibits efficient replication ex vivo and transmission in vivo. *Science* **370**, 1464–1468. (doi:10.1126/science.abe8499)
50. Smith AM, Adler FR, Perelson AS. 2010 An accurate two-phase approximate solution to an acute viral infection model. *J. Math. Biol.* **60**, 711–726. (doi:10.1007/s00285-009-0281-8)
51. Sun Z *et al.* 2020 Survival of SARS-COV-2 under liquid medium, dry filter paper and acidic conditions. *Cell Discovery* **6**, 1–4.
52. Chin AWH *et al.* 2020 Stability of SARS-CoV-2 in different environmental conditions. *The Lancet Microbe* **1**, e10. (doi:10.1016/S2666-5247(20)30003-3)
53. Hirose R *et al.* 2022 Differences in environmental stability among SARS-CoV-2 variants of concern: both omicron BA.1 and BA.2 have higher stability. *Clin. Microbiol. Infect.* **28**, 1486–1491. (doi:10.1016/j.cmi.2022.05.020)
54. Shuai H *et al.* 2022 Attenuated replication and pathogenicity of SARS-CoV-2 B.1.1.529 Omicron. *Nature* **603**, 693–699. (doi:10.1038/s41586-022-04442-5)
55. Cameroni E *et al.* 2022 Broadly neutralizing antibodies overcome SARS-CoV-2 Omicron antigenic shift. *Nature* **602**, 664–670. (doi:10.1038/s41586-021-04386-2)
56. Mannar D *et al.* 2022 SARS-CoV-2 Omicron variant: antibody evasion and cryo-EM structure of spike protein–ACE2 complex. *Science* **375**, 760–764. (doi:10.1126/science.abn7760)
57. Zhang J *et al.* 2022 Structural and functional impact by SARS-CoV-2 Omicron spike mutations. *Cell Rep.* **39**, 110729. (doi:10.1016/j.celrep.2022.110729)
58. Metzdorf K *et al.* 2023 TMPRSS2 is essential for SARS-CoV-2 beta and omicron infection. *Viruses* **15**, 271. (doi:10.3390/v15020271)
59. Mautner L *et al.* 2022 Replication kinetics and infectivity of SARS-CoV-2 variants of concern in common cell culture models. *Virol. J.* **19**, 1–11. (doi:10.1186/s12985-022-01802-5)
60. Rudraraju R *et al*. 2022 Parallel use of pluripotent human stem cell lung and heart models provide new insights for treatment of SARS-CoV-2. *bioRxiv*. (doi:10.1101/2022.09.20.508614)
61. Shi G, Li T, Lai KK, Yewdell JW, Compton AA. 2023 Omicron Spike confers enhanced infectivity and interferon resistance to SARS-CoV-2 in human nasal tissue. *bioRxiv*. (doi:10.1101/2023.05.06.539698)
62. Chin AWH, Lai AMY, Peiris M, Poon LLM. 2022 Increased stability of SARS-CoV-2 Omicron variant over ancestral strain. *Emerg. Infect. Dis.* **28**, 1515–1517. (doi:10.3201/eid2807.220428)
63. McCormack CP, Yan AWC, Brown JC, Sukhova K, Peacock TP, Barclay WS, Dorigatti I. 2023 Modelling the viral dynamics of the SARS-CoV-2 Delta and Omicron variants in different cell types. Figshare. (doi:10.6084/m9.figshare.c.6753889)